

Martensitic phase transformation in short-range ordered Fe₅₀Rh₅₀ system induced by thermal stress and mechanical deformation

Esmaeil Adabifiroozjaei^{a,*}, Fernando Maccari^b, Lukas Schäfer^b, Tianshu Jiang^a, Oscar Recalde-Benitez^a, Alisa Chirkova^{b,c}, Navid Shayanfar^b, Imants Dirba^b, Nagaarjhuna A Kani^{a,d}, Olga Shuleshova^e, Robert Winkler^a, Alexander Zintler^{a,f}, Ziyuan Rao^g, Lukas Pfeuffer^b, András Kovács^h, Rafal E. Dunin-Borkowski^h, Konstantin Skokov^b, Baptiste Gault^{g,i}, Markus Gruner^j, Oliver Gutfleisch^{b,†}, Leopoldo Molina-Luna^a

^a Advanced Electron Microscopy, Institute of Material Science, Technical University of Darmstadt, Darmstadt 64287, Germany

^b Functional Materials, Institute of Materials Science, Technical University Darmstadt, Darmstadt 64287, Germany

^c Hochschule Bielefeld – University of Applied Sciences and Arts, Interaktion 1, Bielefeld 33619, Germany

^d Division of Research with Neutrons and Muons, Paul Scherrer Institute, Switzerland

^e The Leibniz Institute for Solid State and Materials Research, Dresden 01069, Germany

^f Karlsruhe Institute of Technology, Laboratory for Electron Microscopy (LEM), Engesserstr. 7, Karlsruhe 76131, Germany

^g Max-Planck-Institut für Eisenforschung, Düsseldorf 40237, Germany

^h Ernst Ruska-Centre for Microscopy and Spectroscopy with Electrons and Peter Grünberg Institute, Forschungszentrum Jülich, Jülich 52425, Germany

ⁱ Department of Materials, Royal School of Mines, Imperial College London, London SW7 2AZ, UK

^j Faculty of Physics and Center for Nanointegration Duisburg-Essen (CENIDE), University of Duisburg-Essen, Duisburg 47057, Germany

ARTICLE INFO

Keywords:

Fe₅₀Rh₅₀

Martensitic transformation

Premartensite

Atomic shuffling

External stress

ABSTRACT

Metallic/intermetallic materials with BCC structures hold an intrinsic instability due to phonon softening along [110] direction, causing BCC to lower-symmetry phases transformation when the BCC structures are thermally or mechanically stressed. Fe₅₀Rh₅₀ binary system is one of the exceptional BCC structures (ordered-B2) that has not been yet showing such transformation upon application of thermal stress, although mechanical deformation results in B2 to disordered FCC (γ) and L1₀ phases transformation. Here, a comprehensive transmission electron microscopy (TEM) study is conducted on thermally-stressed samples of Fe₅₀Rh₅₀ induced by quenching in water and liquid nitrogen from 1150 °C and 1250 °C. We demonstrated that samples quenched from 1150 °C into water and liquid nitrogen show the presence of 1/4{110} and 1/2{110} satellite reflections, the latter of which is expected from phonon dispersion curves obtained by density functional theory calculation. Therefore, it is proposed that Fe₅₀Rh₅₀ maintains the B2 structure that is in premartensite state. Once Fe₅₀Rh₅₀ is quenched from 1250 °C into liquid nitrogen, formation of two short-range ordered tetragonal phases with various c/a ratios (~1.15 and 1.4) is observed in line with phases formed from mechanically deformed (30 %) sample. According to our observations, an accurate atomistic shear model ({110}(1 $\bar{1}$ 0)) is presented that describes the martensitic transformation of B2 to these tetragonal phases.

1. Introduction

FeRh alloys (Fe₅₀Rh₅₀) exhibit an ordered-B2 structure (cubic CsCl-prototype) with an antiferromagnetic (AFM) to ferromagnetic (FM) transition near room temperature [1]. The transition is isostructural

with about 1 % change in volume and is accompanied by giant magnetoresistive and magnetocaloric effects [2]. Therefore, there is great interest in these alloys for various technological applications like heat-assisted magnetic recording (HAMR) [3], antiferromagnetic spintronics [4], and magnetic refrigeration [5,6]. Additionally, there has

* Corresponding author.

E-mail address: e.adabifiroozjaei@aem.tu-darmstadt.de (E. Adabifiroozjaei).

† Oliver Gutfleisch was an Editor of the journal during the review period of the article. To avoid a conflict of interest, Oliver Gutfleisch was blinded to the record and another editor processed this manuscript.

<https://doi.org/10.1016/j.actamat.2023.119577>

Received 23 April 2023; Received in revised form 14 October 2023; Accepted 3 December 2023

Available online 4 December 2023

1359-6454/© 2024 The Authors. Published by Elsevier Ltd on behalf of Acta Materialia Inc. This is an open access article under the CC BY-NC-ND license (<http://creativecommons.org/licenses/by-nc-nd/4.0/>).

been particular interest on Fe₅₀Rh₅₀ as a model system to investigate the effect of external fields on the first-order transitions [7].

Since the transition is isostructural, the majority of previous studies did not focus on the local atomic structure characterization of the alloys in either AFM or FM states. The studies that have been conducted so far usually provide an average picture of the structure determined applying high-resolution X-ray diffraction [8], X-ray magnetic circular dichroism [9], X-ray photoelectron spectroscopy, and nuclear resonant inelastic X-ray scattering techniques [2]. Although these techniques benefit from high accuracy, they cannot visualize the local atomic structure and correlated defect structures of FeRh alloy. To this end, scanning transmission electron microscopy (S/TEM) with ability to resolve localized atomic structure could be utilized [10,11].

Detailed TEM studies of FeRh alloys conducted by McLaren [1] evidenced of ordered modulations, when the alloys are observed along [100], [110], and [111] directions. Independent studies also reported similar and unique superlattice reflections in the [110] zone axis [12,13] in thin films and bulk alloys. On the other hand, extensive structural characterization of similar systems (Zr [14], Ti [15], Ni-Al [16], CdAu [17], TiN [18], CuZn [19], CuAlNi [19], Ni₂FeGa [20] etc., all having BCC structure) showed presence of premartensite structure before martensite transformation. The premartensite structure manifests itself with usually non-commensurate superlattice reflections in the reciprocal space, while in real space it appears as ordered modulations. According to Zener's theory [21], the ordered-B2 structures (called also β -series of alloys) show softening in elastic constant C' (corresponding to {110}<110> shear modulus) when the temperature is lowered. Such softening in C' yields an anisotropic factor ($A = C_{44}/C'$) leading to an ordered displacement of atoms along [110] and consequent appearance of ordered modulations [22]. In order to see if such softening occurs in FeRh alloy or not, comparison of elastic constants is necessary. However, experimental data for single crystals is not available in the literature due to difficulty in growth of FeRh single crystal. Yet, there has been a recent density functional theory (DFT) calculation on the elastic constants of FeRh alloy, from which the A is reported to be 5.4 for AFM state [23]. This can be compared with the values from similar alloys (NiTi (2), NiAl (9), AuCd (14–11)) [22], implying that, from the point of view of the anisotropy of the elastic constants, a premartensitic structure is expected in FeRh system.

However, to the authors' knowledge, there have been no reports of premartensite structure in binary FeRh system. Nonetheless, when FeRh is alloyed with Pd [24] or Pt [25], ordered tetragonal structures (L1₀) appear. Furthermore, recent detailed DFT calculations made it clear that B2 structure in AFM state is not the ground state in the FeRh system [2,8,23,26–28]. In fact, it was shown that there are imaginary soft modes in the phonon dispersion band of ordered-B2 and when they are fully relaxed, lower symmetry structures such as orthorhombic or monoclinic are obtained. Although monoclinic structure was never observed, the orthorhombic one was stabilized in epitaxially strained film of FeRh on tungsten substrate [8], and the magnetic properties of such disordered orthorhombic structure are deteriorated relative to B2. Additionally, it is also known that electrically-induced strain can control the AFM to FM transition in a reversible manner [9].

Apart from the effect of epitaxial strain on the structure and property of FeRh system, it is also known that plastic deformation of FeRh alloy can induce B2 to L1₀ ($c/a \sim 1.15$) and γ transformation, the latter of which is known to be disordered and displaying spin-glass-like behaviour [12,29–31]. In contrast, γ obtained from dealloying process is in ferromagnetic state at room temperature [32]. The γ is known to transform back to B2 upon heating at ~ 150 °C or higher [30,33]. Interestingly the magnetic properties of B2 structure (AFM to FM transformation) can also be recovered upon the heating. Since diffusion is limited at such low temperature, it is not really known how a disordered phase can be transformed to an ordered phase (B2). Yavari et al. suggested that L1₀ and γ phases have probably short-range order (SRO)

and that is why they show spin-glass-like behaviour [30]. However, still there is no concrete description of transformation mechanism for mechanically stressed FeRh alloy. Additionally, it is yet not elucidated how FeRh alloy respond to thermal stress (caused by quenching from high- to low-temperatures), as it is known to also cause displacive transformation [34].

In order to shed light on the effect of thermal and mechanical stresses on the microstructural and magnetic properties of Fe₅₀Rh₅₀ alloy, the present study used S/TEM techniques to comprehensively study the local atomic structure of Fe₅₀Rh₅₀ alloys that were thermally and mechanically stressed. Three types of thermally-stressed samples were examined: (1) quenched from 1150 °C into water, (2) quenched from 1150 °C into liquid nitrogen (LN₂), (3) and quenched from 1250 °C into LN₂. The latter is compared with a mechanically deformed (30 % plastic deformation) sample. From the data acquired in samples 1 and 2, it was observed that there are satellite reflections at 1/4 and 1/2 of {110} plane reflections related to slight atomic displacement of both Fe and Rh along {110} planes. Additionally, our DFT calculation predicted phonon softening at reciprocal points $>1/2[\bar{1}10]$. Accordingly, it was proposed that these samples are in a premartensite state. In contrast, sample 3 showed two L1₀ phases with different c/a ratio (~ 1.15 and 1.4). These phases also formed in mechanically stressed sample. A shuffling mechanism was proposed that describes perfectly the B2 to these L1₀ structures transformation. Overall, our results indicate that FeRh B2 structure has an intrinsic instability which causes its transformation to lower symmetry structures induced by thermal or mechanical stress.

2. Experimental procedure

The ingot with the composition Fe₅₀Rh₅₀ was prepared by arc melting of the appropriate amounts of pure Fe (99.995 %, Alfa Aesar) and Rh (99.9 %, Alfa Aesar) in a water-cooled Cu-crucible. The sample was melted 3 times to ensure homogeneity, after which it was suction-cast in a 2-mm rod. The rod was cut to thin plates of the approximate thickness of 0.5 mm for subsequent heat treatment. The chemical composition of alloy was determined (Fe: 50.11, Rh: 49.89 at%) using inductively coupled plasma (ICP) spectroscopy. The samples were sealed in quartz tubes under pure Ar atmosphere (0.2 bar) and were subjected to annealing to obtain the ordered-B2 phase. The annealing was done at 1150 °C for 72 h followed by water quenching. The tube was not broken in order to prevent oxidation. Slow cooling was also tested from 1150 °C with cooling rate of 0.1°/min. For thermal quenching in LN₂,¹ the samples were encapsulated in quartz tubes backfilled with Ar and quenched from 1150 °C and 1250 °C (with dwelling time of 3 h) into LN₂. In this process, the tube was broken in order to let the alloy quickly reach LN₂ temperature. Afterwards, the surface of the samples was finely polished and room temperature X-ray diffraction was recorded using a Bruker D8 advance diffractometer in Bragg-Brentano geometry with Cu K-alpha radiation and energy dispersive detector. A step size of 0.02° was used and the sample was continuously rotated during the measurement. Thermomagnetic measurements were carried out using a vibrating sample magnetometer (VSM) in a magnetic property measurement system (MPMS3, Quantum Design USA) under applied field ($\mu_0 H_{app}$) of 1 T. Heating and cooling curves were recorded within a temperature range between 10 K and 450 K with temperature rate of 2

¹ Along with quenching in the water, liquid nitrogen quenching is sometimes particularly beneficial for certain applications where superior performance is essential. The exceptionally high quenching rate obtained in this method is primarily due to the low temperature of LN₂. Despite its modest thermal conductivity (compared to water and other quenching mediums), the relatively high heat capacity and a phase change from a liquid to a gas (vapor) when liquid nitrogen comes into contact with a hot metal surface, make the liquid nitrogen quenching more advantageous than the conventional water quenching.

K/min. Mechanical deformation was done using Instron Universal Test Machine.

For TEM investigations, electron transparent thin sections were prepared using various methods. Most of the lamella were prepared conventionally using mechanical polishing for initial thinning and subsequent Argon milling by precision ion polishing system (PIPS: Gatan Dual Ion Mill Model 600) to create small hole in the sample. For initial PIPS process, an angle of 4° and energy of 4.5 KeV were used. Final milling was done using angle of 1.5° and energy of 2 keV. Milling at LN_2 temperature. Focused ion beam (FIB: JEOL JIB-4600F) milling using Ga ion also was used. Initial and final milling energies were set to 30 kV and 2 kV, respectively. Regardless of the method to prepare lamella, similar nanostructural features were observed in FeRh alloy.

The TEM investigation was done using JEM-2100, JEOL machine while STEM observations were made by aberration corrected JEM-ARM200, JEOL, FEI Titan 80–200 (ChemiSTEM) and FEI Titan Tecna G2 F20 machines. In TEM mode, bright-field, dark-field, and high resolution TEM images were acquired, while selected area diffraction pattern was used to characterize the structure. In STEM mode, high-angle annular dark-field (HAADF) images were recorded using a detector semi-angle of $90\text{--}370$ mrad. STEM image simulations in this study were performed using multislice algorithm via prismatic [35,36] software. The probe size used for the simulations was $0.5 \text{ \AA} \times 0.5 \text{ \AA}$, and the semi-angle was set to 30 mrad. To obtain the simulated HAADF-STEM images, we selected the inner and outer virtual detectors as 90 mrad and 125 mrad, respectively. The diffraction pattern simulation was done using CrysTBox (Crystallographic Toolbox). The visualization of crystal structure was performed using VESTA (Visualization for Electronic and Structural Analysis) [37]. The nano-scale elemental distributions in the alloys were investigated by atom probe tomography (APT) (LEAP 5108XR, Cameca Inc.) at a pulse repetition rate of 200 kHz and a pulse energy of 80 pJ. The operating temperature was 60 K and the target detection rate was set to five ions detected every 1000 pulses. Site-specific lift-out of APT tips was performed from the homogenized

and annealed alloys with a FIB instrument (an FEI Helios Plasma focused ion beam (PFIB)) [38–40].

The calculation of the phonon dispersion relations were carried out as described in [2] within the so-called direct or approach using the PHON code [41] to diagonalize the dynamical matrix. Force constants were obtained from density functional theory (DFT) calculations involving ionic displacements of 0.02 \AA in a $3 \times 3 \times 3$ supercell constructed from the 4-atom primitive cell with fcc basis describing the antiferromagnetic ground state structure. For this step, we employed the plane wave code VASP [42,43] in combination with the generalized gradient approximation for exchange and correlation in the formulation of Perdew, Burke and Ernzerhof [44]. We used projector augmented wave [43] potentials with 3p, 3d, and 4 s valence states for Fe and 4p, 4d, and 5 s for Rh together with a plane wave cutoff $E_{\text{cut}}=450$ eV. Brillouin zone integration was carried out on a $4 \times 4 \times 4$ Monkhorst-Pack k-grid in combination with a finite temperature smearing according to Methfessel and Paxton [45] with a broadening of 0.1 eV.

3. Results and discussion

3.1. The premartensite structure

(1) Quenching from 1150°C into water

Fig. 1a–c show the electron diffraction patterns of sample 1 along three principal zone axes ($[001]$, $[\bar{1}\bar{1}0]$, $[\bar{1}\bar{1}1]$), while Fig. 1d–f show the HRTEM images of the sample along the corresponding directions. The main reflections in all three zone axes match the B2 structure. However, there is a systematic presence of extra reflections (marked with dashed yellow circles) and in HRTEM corresponding modulations (marked with dashed yellow lines) along $\{100\}$ and $\{110\}$ planes reflections. The extra reflections can be inclined from the main reflections with angles smaller than 15° (Fig. 1b and c) or sometimes

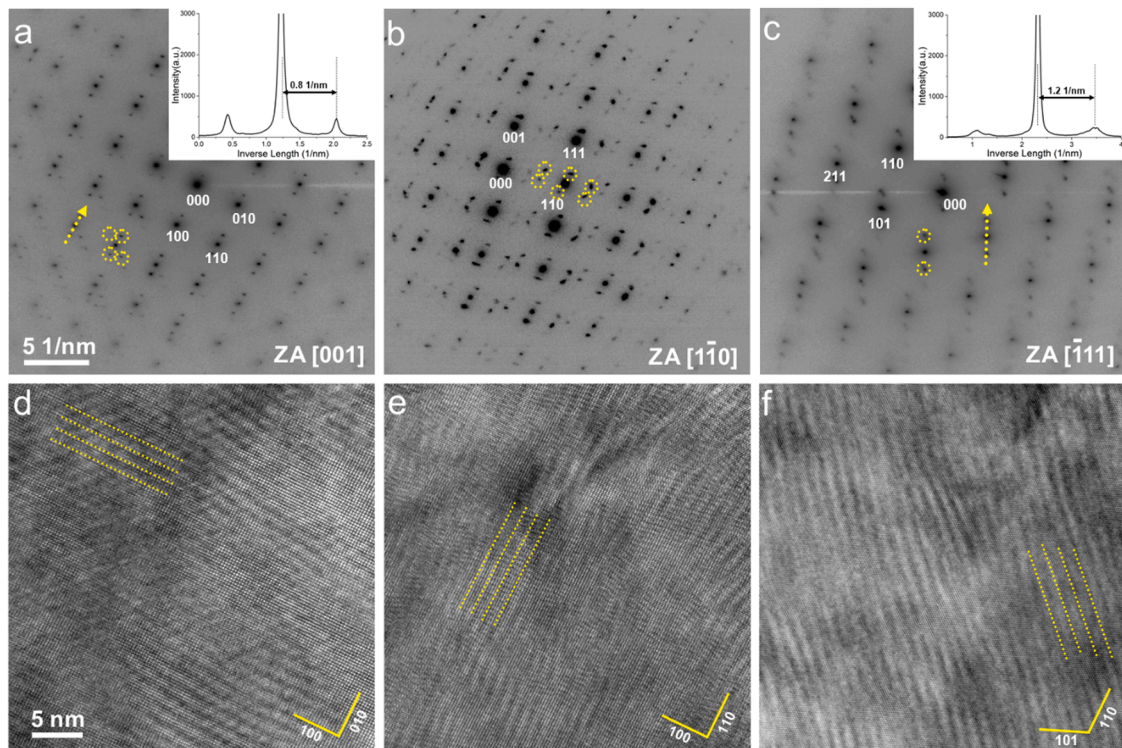


Fig. 1. TEM electron diffraction patterns (a–c) and corresponding HRTEM images (d–f) of FeRh alloy in three principal zone axes. The dashed circles in (a–c) show the satellite reflections. The insets in a and c are intensity scan recorded from the dashed arrows showing the distance of modulations from main reflections. Dashed lines in d–f highlight the modulations.

aligned closely with the main reflections (Figs. 1a and S1). The spacing of the modulations, as shown in inset of Fig. 1a and b are ~ 0.8 for $\{100\}$ plane and 1.2 $1/\text{nm}$ for $\{110\}$ plane. These are located at $\sim 1/4$ of $\{100\}$ and $\{110\}$ planes reflections. The spacing of these modulations varies between 0.6 and 0.8 $1/\text{nm}$ for modulation along $\{100\}$, while that for modulation along $\{110\}$ varies in the range of 1.0 – 1.2 $1/\text{nm}$, meaning that they are incommensurate. These variations were consistently observed on different domains within the same sample and in different samples. Interestingly, each domain has different modulations as shown in Fig. S2. The size of each domain can be as large as few hundred nanometres, while the grain size in the sample ranges between a few to tens of micrometre. Two previous studies reported extra reflections at $[1\bar{1}0]$ zone axes [12,13], as shown in Fig. S3. Using dark-field imaging, Takahashi et al. [12] stated that the extra reflections are caused by fine nanoprecipitates of the γ phase formed during cold rolling, and Castiella et al. [13] supported this hypothesis. However, Castiella's thin films were annealed at 700°C for 6 h, sufficient for transforming γ to B2 [33]. Additionally, the spacings of these extra reflections do not match with those expected for the γ phase. Additionally, the X-ray pattern (Fig. S4) of the present sample showed no trace of γ phase after quenching from 1150°C into water, while in the as-cast state the presence of γ reflections is clear.

In order to examine the variation in chemical composition, atom probe tomography measurements were carried and the results are presented in Fig. S5. Although there is slight variation in chemical composition as the 1D chemical composition shows (Fig. S5d), but this cannot be related to the modulation observed in the sample as the frequency of the chemical composition change (~ 6 nm) is much longer than that observed in the sample (~ 1 nm). To further study the origin of the extra reflections dark-field (DF) TEM imaging was applied, revealing a modulated nanostructure as shown in Fig. 2a and b. It worth noting that no trace of γ phase in the matrix of B2 ordered phase was found. In order to clarify if the quenching in water resulted in the modulated nanostructure, the same alloy was slowly cooled ($0.1^\circ/\text{min}$ from 1150°C). The diffraction pattern in Fig. S6 reveals modulations in the nanostructure. A comparison of the magnetic properties of both alloys, quenched in water and slow-cooled, was performed and the results are presented in Fig. 2c. The transition temperature is slightly higher for the slow-cooled alloy than that quenched in water, but both samples show very sharp transition. These observations evidence that the extra reflections are a fingerprint of FeRh alloy (at least for $\sim 50/50$ alloys) with a B2-ordered structure.

As mentioned before, such modulated structures were observed in similar alloys and they were ascribed to phonon softening in $[110]$ directions. For example, in NiTi alloys [22] or stoichiometric Ni_2MnGa [46], the phonon softening is manifested at $\sim 1/3\text{TA}2[\zeta\zeta 0]$ (transverse acoustical) and hence extra reflections appear at $\sim 1/3$ of $\{110\}$ planes reflections in reciprocal spaces. Therefore, in $\text{Fe}_{50}\text{Rh}_{50}$ system, if the observed modulations are related to phonon softening then very low phonon frequencies or minimums should be present at $\sim 1/4\text{TA}2[\zeta\zeta 0]$ and $\sim 1/4\text{TA}1[\zeta 00]$. Unfortunately, there is only one experimental report of inelastic neutron spectroscopy measurement of FeRh, which is not very conclusive [47]. Hence, density functional theory (DFT) calculation was carried out to produce phonon dispersion curves for AFM state of FeRh. The phonon dispersion curves along $[\zeta\zeta 0]$ and $[\zeta 00]$ were obtained and given in Fig. 2d. As seen, all branches start to show low frequencies or even minimums when ζ is larger than $1/2[\zeta 00]$ or $1/2[\zeta\zeta 0]$. Additionally, the frequency for boundary of $\text{TA}1[\zeta 00]$ and $\text{TA}2[\zeta\zeta 0]$ zones approach negative values, implying that the B2 structure in AFM state is not stable. Another interesting fact is the very low frequency observed for the whole $\text{TA}2[\zeta\zeta 0]$ branch, while for ζ larger than $1/2$ the value starts to become close to zero. From the current DFT data, one can infer that the B2 structure should show extra reflections at points larger than $1/2\text{TA}2[\zeta\zeta 0]$ and $\sim 1/2\text{TA}2[\zeta 00]$, while the current TEM data present extra reflections at $\sim 1/4\text{TA}2[\zeta\zeta 0]$ and $\sim 1/4\text{TA}1$

$[\zeta 00]$. However, it has to be considered that DFT calculation is done at zero Kelvin, whereas the TEM data is collected at room temperature. Furthermore, in similar studies on Zr and Ti metals [14,48], very low frequencies (not minimum) were observed at $\sim 1/2\text{TA}2[\zeta\zeta 0]$. This is known to be responsible for instability of BCC structure which finally causes displacement of atoms along $[110]$ and turning BCC to hexagonal (HCP).

To gain insight about the cause of the $\sim 1/4\{110\}$ reflection, high resolution HAADF-STEM imaging along $[001]$ was carried out. Fig. 3a–c are HAADF images of same area at different magnifications. Fig. 3a (also the inset) and b show that the modulation is uniformly present in the nanostructure while it has slight deviation from (110) plane reflection. Fig. 3c provides a closer look at the nanostructure, in which now it is possible to observe that in some portions of the nanostructure Fe and Rh atoms are smeared out relative to the other atoms and these are in fact the areas that form the modulated structure. To clarify this further, line profile along 5 lines in the Fig. 3c were analysed. According to the B2-ordered structure, the atomic profile for line 1, 3, and 5 should be same, while same is true for lines 2 and 4. These line profiles are plotted in Fig. 3e. While line profiles of 1 and 5 are both sharp and very alike, line 3 shows a smeared-out profile. On the other hand, line profiles of 2 and 4 reveal another interesting feature, which is a relative shift (0.3 \AA) in Fe and Rh peaks. These results indicate that the modulated structure in the B2-ordered structure is due to displacement of atoms in (110) along $[1\bar{1}0]$, while the shift directions are different for different atomic rows. Based on the acquired information, a supercell with some atoms displaced about 0.3 \AA is prepared. The schematic of supercell is shown as Fig. S7, while the result of HAADF-STEM image simulation on the supercell is given as Fig. 3d. In order to accurately evaluate the structure, 5 line-profiles were made like in Fig. 3c and the results are shown as Fig. 3f. A good agreement of line profiles in Fig. 3e and f were obtained. Furthermore, theoretical diffraction pattern of the prepared supercell along $[001]$ was simulated (see Fig. S8). The resemblance of the simulated diffraction pattern and the FFT image (inset in Fig. 3a) is very high. It should be also noted that the length of displacement, which determines the intensity of the extra reflection, is not uniform all over the sample. As an example, Fig. S9 shows a HAADF-STEM image taken from another sample along the $[001]$ crystallographic direction. As the HAADF image and corresponding FFT image show, the modulation is not easily visible.

To study the atom displacements from different viewing angles, HAADF-STEM studies were carried out on FeRh grains with $[\bar{1}11]$ zone axis orientation. Fig. 4a and the corresponding FFT pattern (inset) confirms that the modulation is also present in this direction. Fig. 4b shows a high-resolution HAADF-STEM image of the same region. Similar to what was observed in Fig. 3a, the modulation seems to be caused by smearing of some atomic columns (yellow small arrows Fig. 4b). The inset in Fig. 4b, which is the line profile along dashed-yellow arrow, also reveals that the intensities of some atomic columns are lower than others. This can be attributed to atomic displacement in (110) plane along $[\bar{1}10]$. In order to see if the displacement matches the observations in $[\bar{1}11]$ as it was previously suggested, a simulated HAADF-STEM image of the proposed structure model along $[\bar{1}11]$ was prepared. However, a perfect match could not be found as it seemed that the displacement of atoms in (110) plane along $[\bar{1}10]$ is not enough to reproduce the observed nanostructure along $[\bar{1}11]$. Hence, the previously prepared supercell was taken as basis and a new supercell was prepared in which the atoms are not only displaced in (110) plane along $[\bar{1}10]$, but also in (100) plane along $[\bar{1}00]$. The schematics of this new supercell in $[001]$ and $[\bar{1}10]$ zone axes are shown in Figs. S10 and S11, respectively. The related cif file (CIF FILE 1) is attached to this manuscript as Supplementary Material 2. The HAADF-STEM image simulation and the simulated diffraction pattern of newly prepared supercell along $[\bar{1}11]$ are shown in Fig. 4c and Fig. S12, respectively. From these results, it can be seen that the HAADF-STEM observation and the simulated

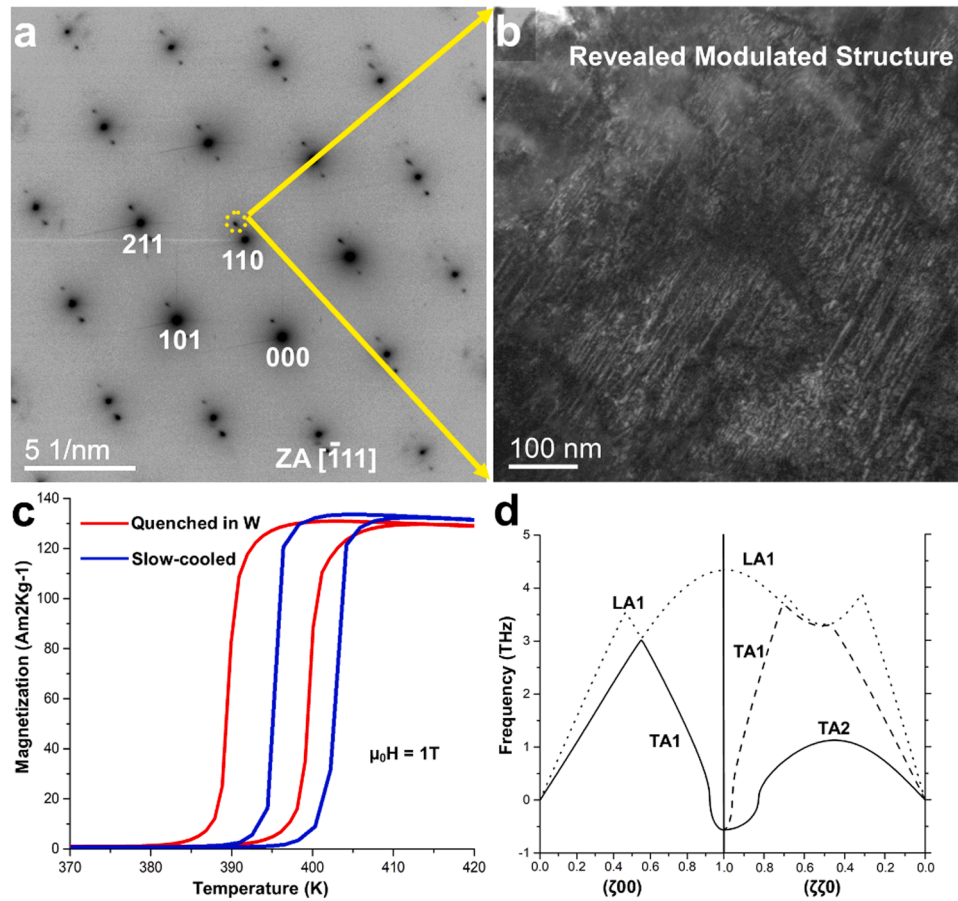


Fig. 2. **a** Electron diffraction pattern taken in $[111]$ zone axis from sample 1 and **b** is a dark-field image recorded using the extra satellite reflection circled by dashed yellow line in **a**. **c** Magnetization vs temperature measurement for alloys cooled through quenching in water (sample 1: red) and with $0.1^\circ/\text{min}$ cooling rate (blue) from 1150°C . **d** Phonon dispersion curves of $\text{Fe}_{50}\text{Rh}_{50}$ alloy (for AFM state) recorded along $[\zeta\bar{1}0]$ and $[\zeta00]$ done at zero Kelvin.

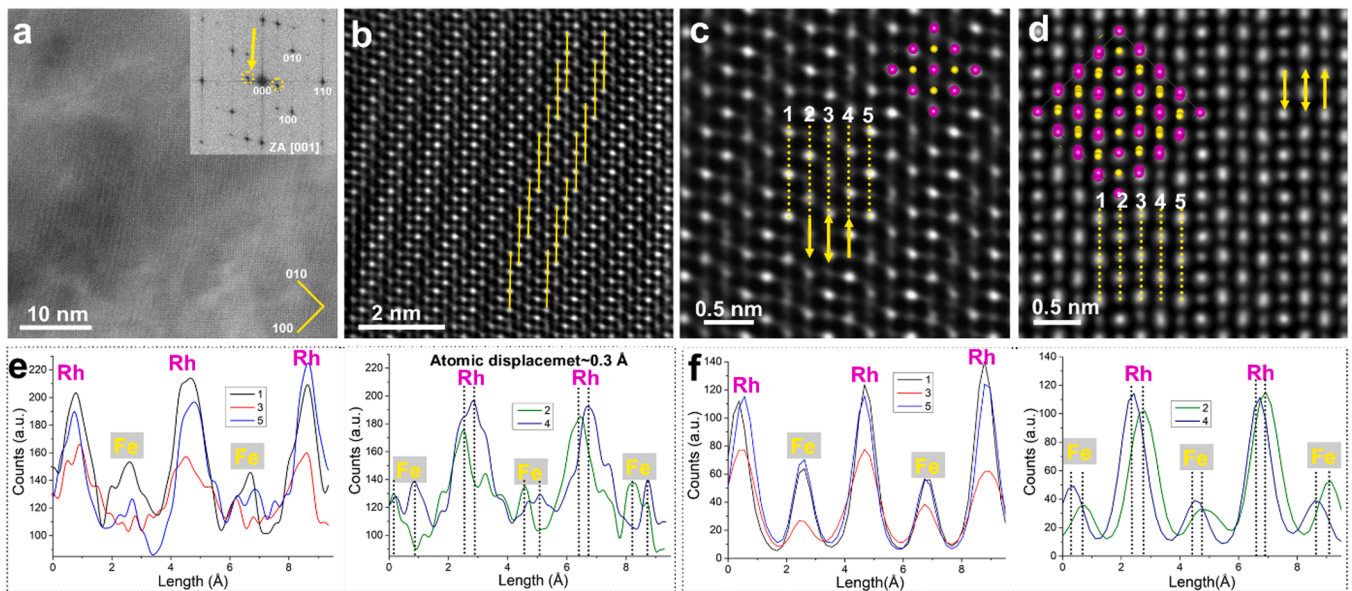


Fig. 3. **a–c** HAADF-STEM images of FeRh alloy along $[001]$ at different scales. Inset in **a** is an FFT pattern of **a**. **d** Simulated HAADF-STEM image using the proposed supercell. **e** is the line profiles for lines 1–5 in **c**. **f** is the line profiles for lines 1–5 in **d**. Arrows in **c** and **d** show direction of atomic displacement. The onset of the axis in **e** and **f** are where the line numbers are written.

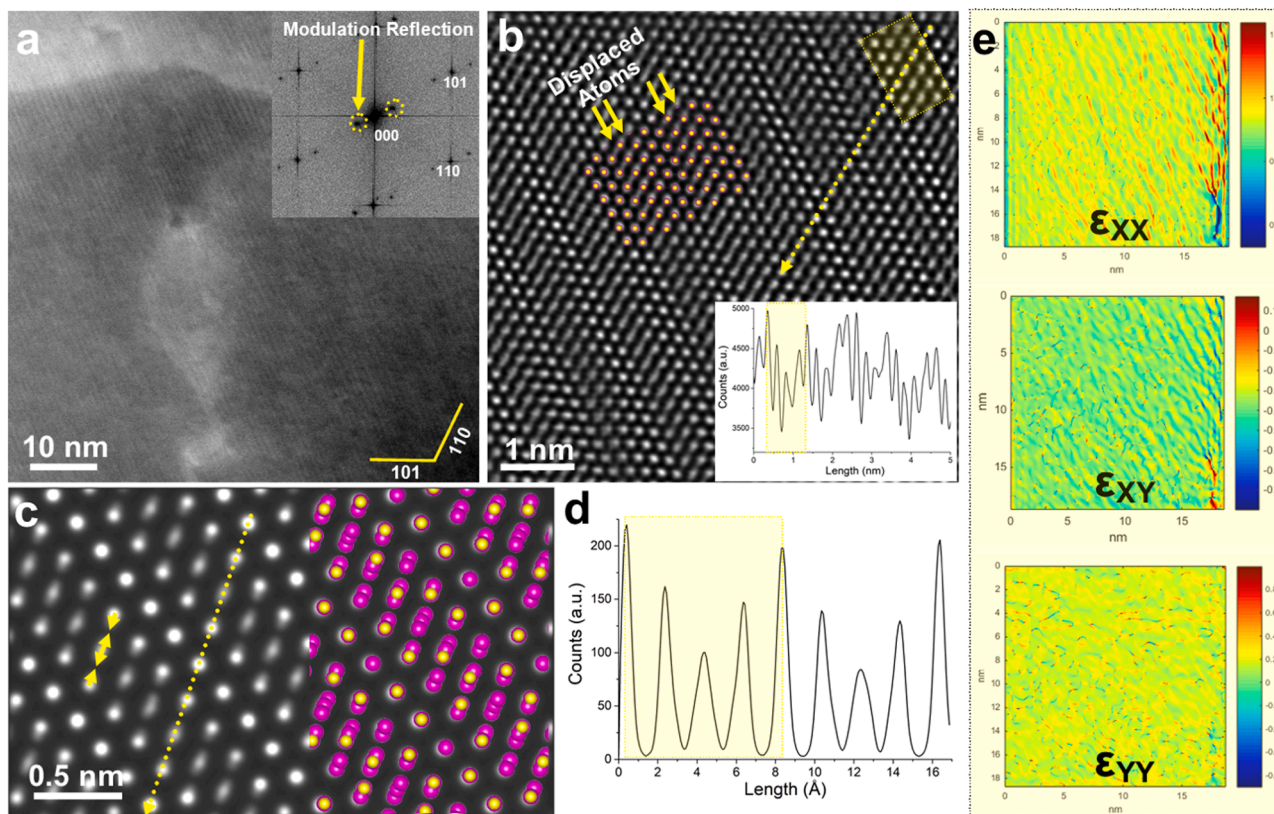


Fig. 4. a and b HAADF-STEM images of FeRh alloy viewed along $[\bar{1}11]$ direction. Inset in a is an FFT pattern recorded from the same region. Inset in b is line profile along dashed arrow. c Simulated HAADF-STEM image that partially overlapped with the proposed supercell (yellow Fe, purple Rh) and d is line profile along dashed arrow in c. Small arrows in c indicate atomic displacement direction. e Strain maps extracted from GPA analysis.

images match closely. Such ordered displacement of atoms is expected to induce localized strain in the nanostructure. The strain can be visualized by applying the geometrical phase analysis (GPA)² on HAADF-STEM images. The image that was used for GPA analysis is shown as Fig. S13. The results of the GPA analysis that are presented in Fig. 4e, clearly indicate that the strain accommodation (ϵ_{xx} and ϵ_{yy} particularly) in the nanostructure is well-aligned with the displacement modulation. Thus, it can be concluded that the observed modulation is caused by ordered atomic displacement in $\{110\}$ and $\{100\}$ planes and, as expected these modulations are correlated to strain accommodation in the structure. Such modulated structures are commonly observed in unary, binary, ternary alloys with BCC structures and is known to be a pre-martensite structure state as mentioned in the Introduction.

(1) Quenching from 1150 °C into liquid nitrogen

In order to investigate the effect of the thermal stress on the nanostructure of FeRh alloy and its magnetic properties, quenching in LN_2 from 1150 °C was performed. Interestingly, as seen in Fig. 5a, the magnetic properties of the alloy changed considerably after quenching in LN_2 , showing a large ferromagnetic background at low temperature. To correlate the ferromagnetic background with a possible phase transition, XRD and TEM examinations were carried out. The XRD pattern (Fig. 5b) does not show formation of any new phase. In line with this, electron diffraction pattern of the alloy (Fig. 5c) only shows presence of the B2-ordered structure. Yet, a closer look at the pattern reveals a new set of satellite reflections appearing at $\sim 1/2\{110\}$ plane reflections, as

shown by Fig. 5d (See also Fig. S14). From the DFT calculation, it was expected to observe extra reflections at such points, since very low frequency phonons were observed at points larger than $1/2\text{TA}_2[\zeta\zeta 0]$. Fig. 5e is an HRTEM image taken from the alloy (in $[001]$ zone axis) which show nearly parallel domains in the nanostructure. Image filtering using FFT was carried out by selecting two of these $1/4\{110\}$ planes reflections (1 and 2 as indicated in Fig. S14) which reveals that these domains are indeed areas with different displacement modulations. An overview TEM image of the domains in the same zone axis is given in Fig. S15a, indicating that two $1/4(110)$ planes reflections (1 and 2 in Fig. S14) are perpendicular to two $1/4(1\bar{1}0)$ planes reflections (3 and 4 in Fig. S14). The lamella was also examined in $[0\bar{1}1]$ zone axis and the domain-like nanostructure was seen as shown in Fig. S15b. It is worth mentioning that such domain-like nanostructure was not reported for FeRh alloys previously.

Regarding the $1/2\{110\}$ planes reflections, HAADF-STEM imaging along $[001]$ zone axis was performed to reveal the cause. Fig. 6a and b show HAADF-STEM image and corresponding FFT pattern, respectively. The latter shows the presence of $1/2\{110\}$ planes reflections, while in the former the modulated structure is not easily visible. Similar to Fig. 2, line profile analysis was done as shown in Fig. 6c and d for line 1–4 in Fig. 6a. Profiles of lines 1 and 3 are perfectly matching, while the same is true for line profiles of lines 2 and 4. The similarity of line profiles in 1 and 3, and 2 and 4 therefore leads to appearance of $1/2\{110\}$ planes reflections. The lower count intensity observed in the line profiles is considered to be related to atomic displacement, similar to that presented in Figs. 3 and 4. The data show that by quenching sample in LN_2 , the length of modulation in real space decreased from four d -spacing of (110) planes (8.48 Å) to two (4.24 Å). However, it should be mentioned that these modulations are found to be incommensurate, so the modulation length change slightly at different places in the nanostructure.

² Geometric phase analysis is a method of digital signal processing used to determine crystallographic quantities such as d -spacing or strain from high-resolution transmission electron microscope images.

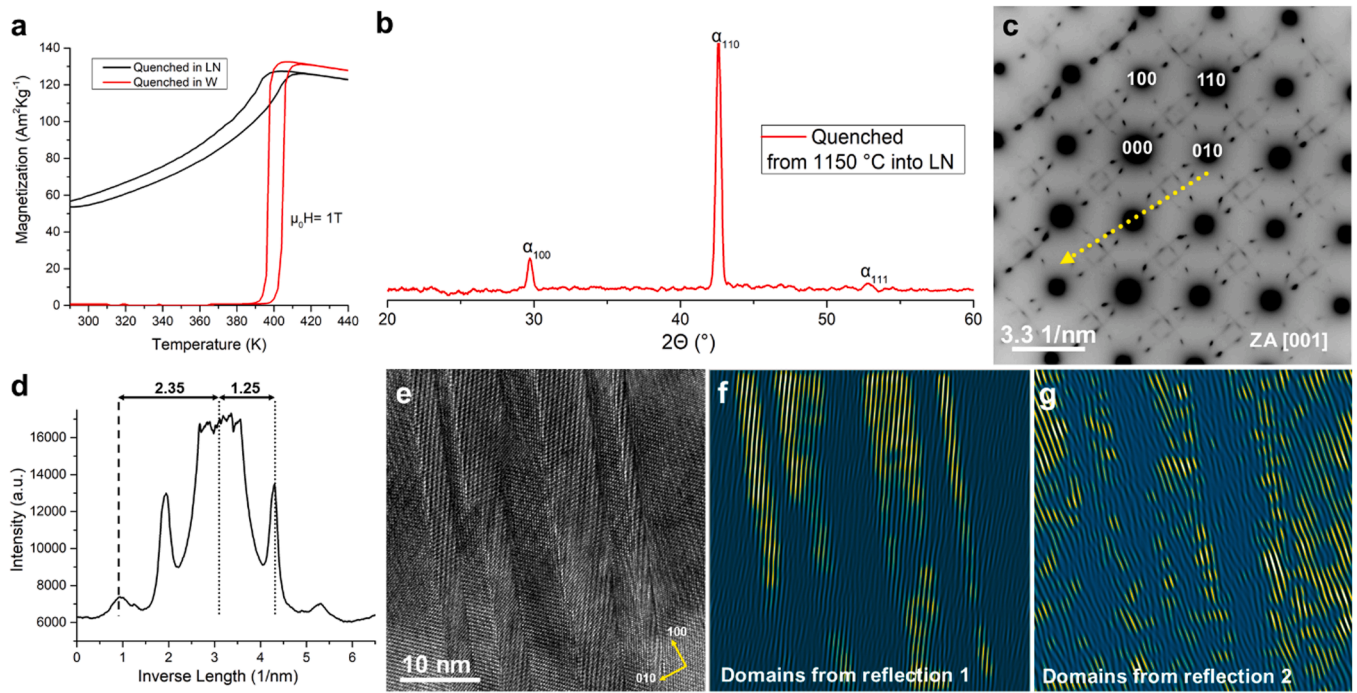


Fig. 5. **a** Magnetization vs. temperature curve for FeRh alloy quenched from 1150 °C into water (red) and LN₂ (black). **b** and **c** XRD and electron diffraction pattern ([001]) of the alloy quenched in LN₂. **d** Line profile recorded along dashed arrow in **c**. **e** HRTEM image of the alloy quenched in LN₂. **f** and **g** Filtered FFT images obtained using satellite reflections (1 and 2) in Fig. S14.

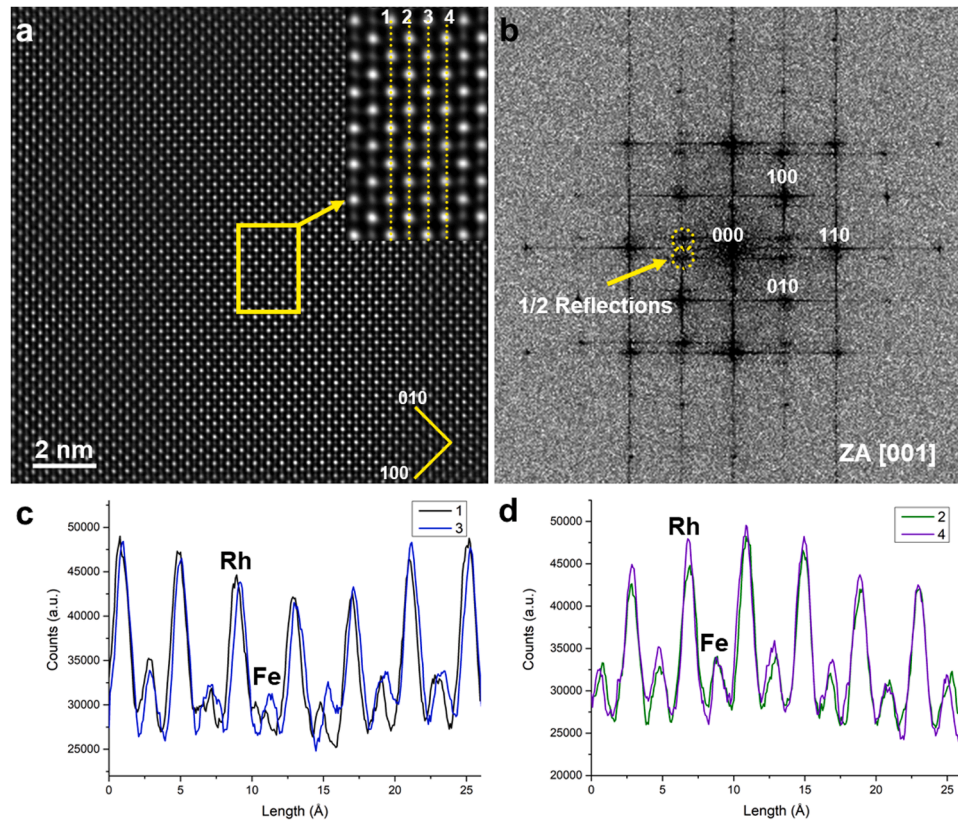


Fig. 6. **a** HAADF-STEM image of areas with $1/2\{110\}$ planes reflections, which can be visibly seen in **b** corresponding FFT image. Inset in **a** is zoomed-in view of yellow rectangle. Line profiles (1–4 in **a**) are given in **c** and **d**.

This is the reason for the $1/2\{110\}$ planes reflections in Fig. 5c appearing streaked. Additionally, quenching in LN_2 from 1150°C resulted in more thermal stress leading to formation of a denser network of slightly different domains (areas in which atoms are displaced slightly in different orientation). Overall, it can be inferred that quenching FeRh alloy from 1150°C into LN_2 causes appearance of premartensite structure, in which portions of atoms are slightly displaced.

(1) Quenching from 1250°C into liquid nitrogen

With the hindsight of the effect of quenching in LN_2 from 1150°C on the alloy, an additional quenching experiment in LN_2 was done, but from 1250°C (at this temperature the alloy has still B2 structure [49]). Fig. 7a shows the XRD measurements of the quenched alloy (black curve). Although the major phase is still B2, additional low intensity but broad peaks are observed at angles $\sim 41^\circ$, 45° and 48° . According to previous reports on mechanical deformation of FeRh alloys [12,30,50,51], these peaks belong to the tetragonal L1_0 ($a = 3.33\text{ \AA}$ and $c = 2.88\text{ \AA}$) and γ ($a = 3.73\text{ \AA}$) phases, respectively. However, a considerable broadening is observed in the peaks, so a distribution of d -spacing is expected. In order to compare the effect of thermal stress with that of mechanical stress on FeRh system, a piece from the same batch of alloy was $\sim 30\%$ compressed (stress-strain curve in Fig. S16) and the obtained XRD pattern is shown in Fig. 7a (red curve). Interestingly, mechanical stressing also results in formation of the same phases. To clarify the nanostructure of the sample quenched in LN_2 , a lamella was prepared using FIB. While preparing the lamella, a two-phase microstructure was observed when the thickness of lamella reached less than one micrometre (Fig. 7b). When lamella was examined in bright-field TEM mode, a two-phase nanostructure was confirmed (Fig. 7c). The diffraction pattern of the dark phase in Fig. 7c was obtained (Fig. 7d) and it was realized that although it seems to be γ [12,30,50,51], but in fact it is a L1_0 structure (tetragonal with c/a ratio of 1.4) that is modulated (see Fig. S17) and has short range order (SRO). It was observed that the 100 and 001 reflections are split as seen more clearly in the low-magnification

HAADF-STEM image and corresponding FFT pattern in Fig. S18a and b. The high-magnification HAADF-STEM image and corresponding line profile are provided as Fig. 7e and f. From these data, c and a are $\sim 3.84\text{ \AA}$ and $\sim 2.78\text{ \AA}$, respectively. It is seen that the order is broken at some boundaries that are basically anti-phase boundaries. In fact, the anti-phase boundaries are the cause of the modulated structure in this phase. It was also observed that there is another L1_0 phase with lower c/a (~ 1.15), the DP of which is shown as Fig. S19. The splitting of 100 and 001 reflections also occurs in this phase and the nanostructure is modulated too. It should be pointed out that these two different L1_0 structures are found to be in the same area with very coherent interfaces. Furthermore, other similar tetragonal structures (less abundant) with slightly different c/a were also observed in the present research that explains the broadness of the XRD peaks. However, since the most abundant tetragonal structures had c/a ratios of ~ 1.15 and 1.4 , the discussion is continued only on these two phases. For simplification, now the L1_0 structures are called $\text{L1}_0\text{l}$ and $\text{L1}_0\text{s}$, l and s standing for longer and shorter c , respectively (see Table 1 for comparison of lattice constants). With the current data, now it is known that the previously-thought disordered γ phase is in fact $\text{L1}_0\text{l}$ structure with SRO. The same is also true for $\text{L1}_0\text{s}$ and therefore the SRO caused the disappearance of 100 and 001 peaks in XRD pattern of the current samples or those in the previous researches [29,51]. The presence of anti-phase boundaries causing the SRO was also reported in other similar systems [52–54]. Overall, from these observations, it is concluded that imposing stress on FeRh B2 structure causes its transformation to L1_0 tetragonal structures with various c/a ratio.

Table 1

The lattice constants (in \AA) of B2, $\text{L1}_0\text{l}$, and $\text{L1}_0\text{s}$ structures.

Phase	a	b	c
B2	2.98	2.98	2.98
$\text{L1}_0\text{s}$	2.89	2.89	3.33
$\text{L1}_0\text{l}$	2.74	2.74	3.84

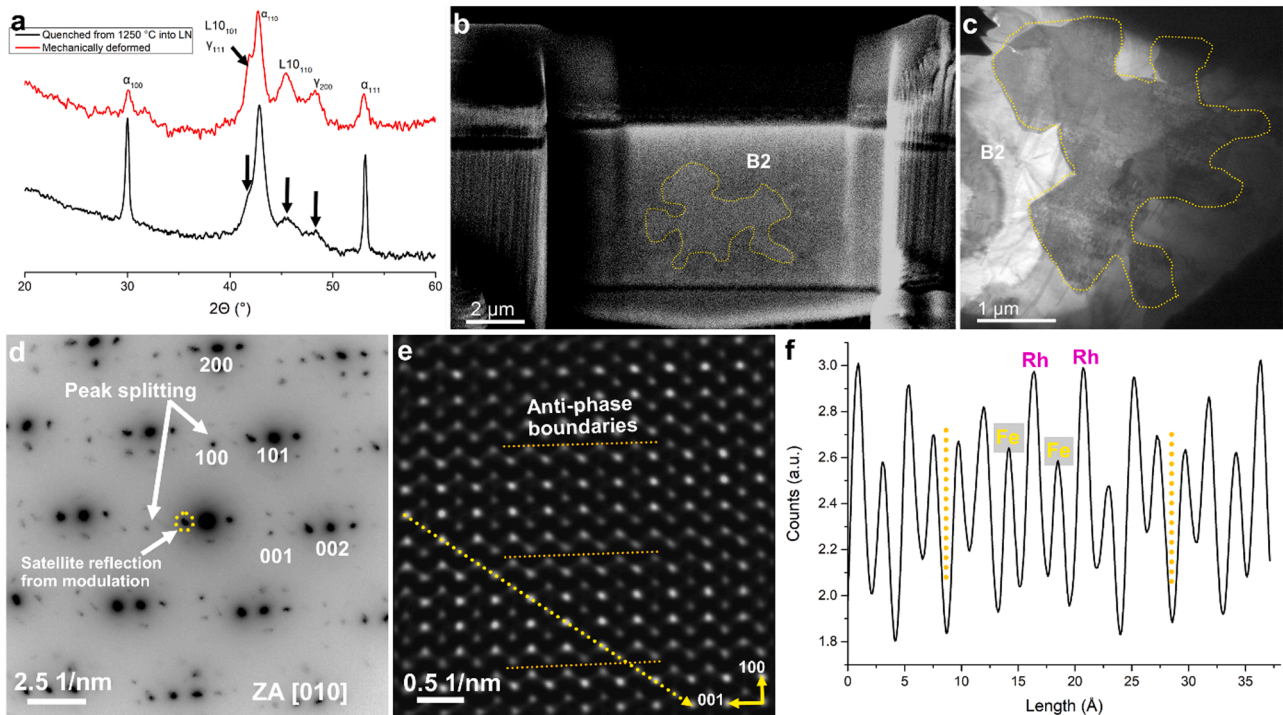


Fig. 7. a XRD measurement of FeRh alloy quenched in LN_2 from 1250°C (black) and alloy mechanically deformed (red). b Secondary electron image of FIB lamella. c Bright-field TEM image taken from alloy quenched from 1250°C into LN_2 . d Electron diffraction pattern and e HAADF-STEM image of $\text{L1}_0\text{l}$ phase viewed along the $[010]$ zone axis. f line profile taken along the dashed arrow in e.

In order to understand the mechanism of B2 transformation to these tetragonal structures an electron diffraction pattern was acquired from the interface of L1₀l and B2 near [001] zone axis of the latter as shown in Fig. S20. As seen, the (−110) plane of B2 is parallel to (101) plane of L1₀, while (101) and (002) form at positions of $\sim 1/2\{110\}$ plane reflections, indicating that the transformation is displacive. Based on the orientation relationship, and according to the displacement mode that was observed in Figs. 3 and 4, an atomic shuffling model that describes the transformation of B2 to L1₀ structures is proposed. Fig. 8a shows the B2 structure along [001], while Fig. 7b and c present the same structure while the atoms are shuffled according to our model to obtain L1₀l and L1₀s, respectively. Such atomic shuffling turns the B2 into L1₀l ([010]) and L1₀s ([010]). The developed model requires shuffling of atoms along one of the {110} planes in opposite or same directions and with different displacement length. The size and direction of arrow determine the length and direction of atomic shuffling. Resultant simulated diffraction patterns of B2, L1₀l, and L1₀s are shown as Fig. 8d, e, and f, respectively. Additionally, superimposition of calculated diffraction pattern of B2 and L1₀l are shown as Fig. S21. When this is compared with experimental diffraction pattern in Fig. S20 a close match can be observed, indicating that our model describes the transformation very well.

The structures obtained in Fig. 8e and f, although being very close to L1₀ structures, but have to be further adjusted in order to exactly resemble the L1₀ structures. The *c* and *a* lattice constants in Fig. 5a are ~ 3.80 Å and ~ 2.36 Å, respectively. While the out of plane spacing (axis *b*) is 2.98 Å, same as B2 structure. Since *c* is very close to what was experimentally observed (3.84 Å) in L1₀l, therefore no significant adjustment is required. However, in order to adjust *a*, the lattice should expand for $\sim 16.5\%$ along [120] in reference to B2 structure as shown in Fig. S22. Also, for the *b*-axis to shrink from 2.98 Å to 2.75 Å, there needs to be $\sim 3.6\%$ shrinkage. This requires atoms to move along the out of plane direction ([001] in B2 structure). These movements are collective, meaning that all atoms are involved. For L1₀s (Fig. 8f), the *a* and *c* are

3.39 Å and 2.65 Å, respectively. Again, *c* is very close to what was observed in experiment (3.33 Å), so no significant adjustment is required. However, in order to get *a* value to 2.80 Å, there needs to be 0.08 % expansion along [430]. For *b* in L1₀s, same adjustment should occur as described for L1₀l.

It is also of importance to discuss the effect of final cooling temperature and cooling rate on martensite formation in the current study. Both of these factors are known to considerably influence the austenite to martensite transformation [55]. A comparison between FeRh and similar systems such as FeC and NiTi can be very insightful in this regard. In FeC, in order to obtain the martensite at room temperature one need to increase the cooling rate as much as possible [56], while in NiTi such high cooling rate is not required [22]. In fact, slow cooling rate can also lead to martensite formation in NiTi system, as clarified by previous *in situ* TEM experiment [57]. In FeC, the mobility of C as small atom should be limited in order to form the martensite [56], while in NiTi system such atom does not exist. Another effect of high cooling rate is the higher thermal stress that consequently leads to accumulation of more strain in the nanostructure. Since there is bond softening in B2 structure of these systems, more strain can facilitate the phase transformation to a great extent. Strain can lead to higher density of defect formation, at site of which nucleation of martensite can occur [58]. In FeRh system, since both atoms are relatively large, therefore the cooling rate can only influence the rate of straining, defect formation and consequently the martensite phase transformation. In the present work, three different quenching experiments were conducted: quenching from 1150 °C into water, quenching from 1150 °C into LN₂, and quenching from 1250 °C into LN₂. Formation of martensite at LN₂ temperature itself indicate that martensite start temperature is indeed close to LN₂ temperature. However, since martensite formation does not occur when quenching is done from 1150 °C into LN₂, it can be concluded that the cooling rate (thermal stress) is possibly not enough for martensite formation, whereas quenching from 1250 °C provide such amount of

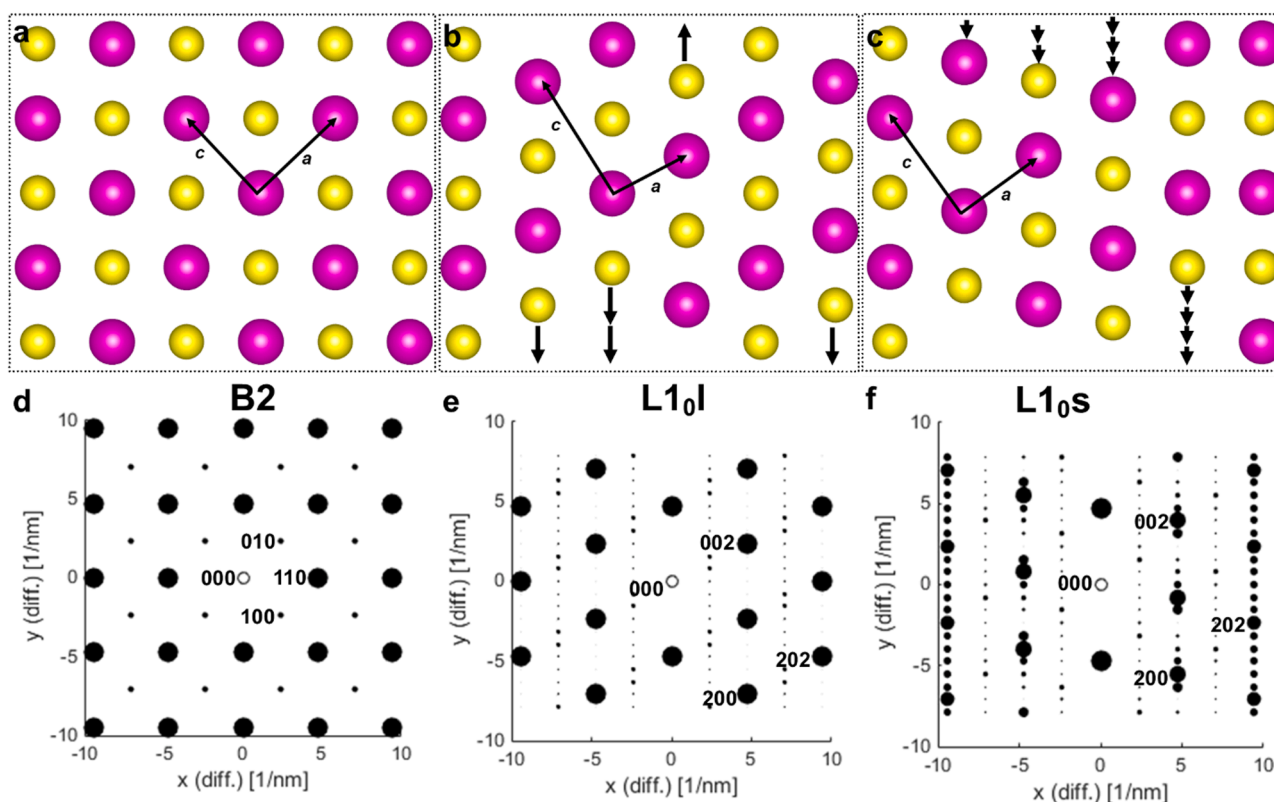


Fig. 8. a–c Atomic models for B2, L1₀l, and L1₀s structures, respectively. Size of arrows in b and c show value and direction of atomic displacement. Larger arrow length value is 1.06 Å, while that for shorter one is 0.53 Å. d, e, and f Calculated electron diffraction patterns of (B2), b (L1₀l), and c (L1₀s) models.

thermal stress. Also, it can be said that the difference between nanostructure observed from quenching in water and LN_2 from 1150 °C is caused by the effect of both cooling rate and final quenching temperature. Cooling from 1150 °C into LN_2 relative to water has ~ 200 °C undercooling difference, therefore there is more thermal stress involved when the sample is quenched in LN_2 . On the other hand, LN_2 temperature is close to martensite start temperature. These factors change the nanostructures and magnetic properties of the alloy to some extent, but are not enough for B2 conversion to tetragonal structures. Overall, it seems that FeRh system require a large extent of cooling rate from a high temperature to LN_2 to transform from B2 to tetragonal phases. Nonetheless, to fully understand the effect of these two factors, a separate comprehensive study is required that could be a topic of further investigation on this system.

4. Conclusion

In the present study, a careful and comprehensive S/TEM study on thermally-stressed $\text{Fe}_{50}\text{Rh}_{50}$ alloy was done and following observations were made:

- (1) For sample quenched in water from 1150 °C, it was observed that there is a systematic satellite reflection at $\sim 1/4\{110\}$ and $1/4\{100\}$ planes reflections that are caused by slight displacement of Fe and Rh atoms in $\{110\}$ and $\{100\}$ planes along $[\bar{1}10]$ and $[\bar{1}00]$, respectively. However, from phonon dispersion curve obtained by DFT satellite reflection at points larger than $\sim 1/2\{110\}$ and $1/2\{100\}$ were expected.
- (2) When sample was quenched from 1150 °C into LN_2 , $1/2\{110\}$ reflections appeared. With the assumption that the atomic structure of the alloy is in frozen state at ~ -167 °C, these reflections meet the expected phonon softening from obtained DFT calculation. It is believed that $1/2\{110\}$ and $1/4\{110\}$ are indications of the premartensitic structures. It should be also mentioned that quenching from 1150 °C into LN_2 did not cause change in B2 structure, but considerably influenced the magnetic properties (broadening of AFM to FM transition).
- (3) Quenching in LN_2 from 1250 °C finally led to B2 phase transformation to two L1_0 structures with different c/a ratio (~ 1.15 and 1.4). The mechanically compressed alloy ($\sim 30\%$) also showed formation of these two tetragonal phases, leading to conclusion that imposing external stress on FeRh alloy results in B2 transformation to tetragonal phases. TEM investigation of the L1_0 structures presented that both are short-range ordered and modulated. Modulations are caused by anti-phase boundaries, in which the order is broken. This explained the absence of 100 and 001 (ordering peaks) in the current and previous studies, misleading researchers to conclude that γ disordered phase is the final martensitic product.
- (4) From the S/TEM observations a model is proposed that describes the martensitic transformation of B2 to these tetragonal structures. Our model requires mainly shear mode of $\{110\}\langle 1\bar{1}0\rangle$.
- (5) According to the results of current study, it is concluded that B2 structure of FeRh in AFM states has intrinsic instability, same as other alloys with B2 structure. Upon exposure of external stress (thermal or mechanical) on FeRh, depending on the extent of the external field, it may transform to two tetragonal phases.

Declaration of Competing Interest

The authors declare that they have no known competing financial interests or personal relationships that could have appeared to influence the work reported in this paper.

Acknowledgment

All authors acknowledge the financial support of German Science Foundation (DFG) in the framework of the Collaborative Research Centre Transregio 270 (CRC-TRR 270, project number 405553726, sub-projects Z01, Z02, A01, A10, B06). ZR and BG acknowledge support from the DFG through the award of the Leibniz Prize 2020. EA also acknowledge David Koch and Alex Aubert for their helpful discussion regarding sample preparation and XRD results.

Supplementary materials

Supplementary material associated with this article can be found, in the online version, at doi:10.1016/j.actamat.2023.119577.

References

- [1] M. McLaren, Transmission electron microscope characterisation of iron-rhodium epilayers, PhD thesis, University of Leeds, 2014.
- [2] M. Wolloch, M.E. Gruner, W. Keune, P. Mohn, J. Redinger, F. Hofer, D. Suess, R. Podlucky, J. Landers, S. Salamon, F. Scheibel, D. Spodig, R. Witte, B. Roldan Cuenya, O. Gutfleisch, M.Y. Hu, J. Zhao, T. Toellner, E.E. Alp, M. Siewert, P. Entel, R. Pentcheva, H. Wende, Impact of lattice dynamics on the phase stability of metamagnetic FeRh: bulk and thin films, *Phys. Rev. B* 94 (2016), 174435, <https://doi.org/10.1103/PhysRevB.94.174435>.
- [3] D. Weller, G. Parker, O. Mosendz, E. Champion, B. Stipe, X. Wang, T. Klemmer, G. Ju, A. Ajan, A HAMR media technology roadmap to an areal density of 4 Tb/in², *IEEE Trans. Magn.* 50 (2014) 1–8, <https://doi.org/10.1109/TMAG.2013.2281027>.
- [4] T. Jungwirth, X. Marti, P. Wadley, J. Wunderlich, Antiferromagnetic Spintronics *Nat. Nanotechnology* 11 (2016) 231–241, <https://doi.org/10.1038/nnano.2016.18>.
- [5] B. Yu, M. Liu, P.W. Egolf, A. Kitanovski, A review of magnetic refrigerator and heat pump prototypes built before the year 2010, *Int. J. Refrig.* 33 (2010) 1029–1060, <https://doi.org/10.1016/j.ijrefrig.2010.04.002>.
- [6] A. Chirkova, K.P. Skokov, L. Schultz, N.V. Baranov, O. Gutfleisch, T.G. Woodcock, Giant adiabatic temperature change in FeRh alloys evidenced by direct measurements under cyclic conditions, *Acta Mater.* 106 (2016) 15–21, <https://doi.org/10.1016/j.actamat.2015.11.054>.
- [7] L.H. Lewis, C.H. Marrows, S. Langridge, Coupled magnetic, structural, and electronic phase transitions in FeRh, *J. Phys. Appl. Phys.* 49 (2016), 323002, <https://doi.org/10.1088/0022-3727/49/32/323002>.
- [8] R. Witte, R. Kruk, M.E. Gruner, R.A. Brand, D. Wang, S. Schlabach, A. Beck, V. Provenzano, R. Pentcheva, H. Wende, H. Hahn, Tailoring magnetic frustration in strained epitaxial FeRh films, *Phys. Rev. B* 93 (2016), 104416, <https://doi.org/10.1103/PhysRevB.93.104416>.
- [9] R.O. Cherifi, V. Ivanovskaya, L.C. Phillips, A. Zobelli, I.C. Infante, E. Jacquet, V. Garcia, S. Fusil, P.R. Briddon, N. Guiblin, A. Mougin, A.A. Únal, F. Kronast, S. Valencia, B. Dkhil, A. Barthélémy, M. Bibes, Electric-field control of magnetic order above room temperature, *Nat. Mater.* 13 (2014) 345–351, <https://doi.org/10.1038/nmat3870>.
- [10] X. Song, T. Ma, X. Zhou, F. Ye, T. Yuan, J. Wang, M. Yue, F. Liu, X. Ren, Atomic scale understanding of the defects process in concurrent recrystallization and precipitation of Sm-Co-Fe-Cu-Zr alloys, *Acta Mater.* 202 (2021) 290–301, <https://doi.org/10.1016/j.actamat.2020.10.067>.
- [11] P.S. Phani, K.E. Johanns, G. Duscher, A. Gali, E.P. George, G.M. Pharr, Scanning transmission electron microscope observations of defects in as-grown and pre-strained Mo alloy fibers, *Acta Mater.* 59 (2011) 2172–2179, <https://doi.org/10.1016/j.actamat.2010.12.018>.
- [12] M. Takahashi, R. Oshima, Stress induced phase transition of iron-rhodium alloys, *J. Phys. IV* 05 (1995) C8–496, <https://doi.org/10.1051/jp4:1995875>.
- [13] M. Castiella, C. Gatel, J.F. Bobo, N. Ratel-Ramond, R. Tan, M. Respaud, M. J. Casanova, Structural investigation of magnetic FeRh epitaxial films, *Mater. Res. Express* 2 (2015), 086401, <https://doi.org/10.1088/2053-1591/2/8/086401>.
- [14] A. Heiming, W. Petry, J. Trampenau, M. Alba, C. Herzig, H.R. Schober, G. Vogl, Phonon dispersion of the BCC phase of group-IV metals. II. BCC zirconium, a model case of dynamical precursors of martensitic transitions, *Phys. Rev. B* 43 (1991) 10948, <https://doi.org/10.1103/PhysRevB.43.10948>.
- [15] J. Fan, J. Li, Y. Zhang, H. Kou, J. Ghanbaja, W. Gan, L. Germain, C. Esling, The origin of striation in the metastable β phase of titanium alloys observed by transmission electron microscopy, *J. Appl. Crystallogr.* 50 (2017) 795–804, <https://doi.org/10.1107/S1600576717004150>.
- [16] D. Schryvers, L.E. Tanner, On the interpretation of high resolution electron microscopy images of premartensitic microstructures in the Ni-Al β_2 phase, *Ultramicroscopy* 32 (1990) 241–254, [https://doi.org/10.1016/0304-3991\(90\)90002-4](https://doi.org/10.1016/0304-3991(90)90002-4).
- [17] G.R. Barsch, T. Ohba, D.M. Hatch, Landau theory of structural transformations in titanium–nickel and gold–cadmium alloys, *Mater. Sci. Eng. A* 273 (275) (1999) 161–165, [https://doi.org/10.1016/S0921-5093\(99\)00282-8](https://doi.org/10.1016/S0921-5093(99)00282-8).
- [18] Z. Xingzhong, W. Xingfang, K. Tsun, Premartensite Phase transformation in TiNi alloy, *Acta Metall.* 37 (1989) 1783–1790, [https://doi.org/10.1016/0001-6160\(89\)90063-1](https://doi.org/10.1016/0001-6160(89)90063-1).

- [19] K. Otsuka, C.M. Wayman, H. Kubo, Diffuse electron scattering in β -phase alloys, *Metall. Trans. A* 9 (1978) 1075–1085, <https://doi.org/10.1007/BF02652212>.
- [20] H. Nath, G. Phanikumar, Premartensite transition in Ni_2FeGa heusler alloy, *Mater. Charact.* 102 (2015) 24–28, <https://doi.org/10.1016/j.matchar.2015.02.012>.
- [21] C. Zener, Contributions to the theory of beta-phase alloys, *Phys. Rev.* 71 (1947) 846–851, <https://doi.org/10.1103/PhysRev.71.846>.
- [22] K. Otsuka, X. Ren, Physical metallurgy of Ti–Ni-based shape memory alloys, *Prog. Mater. Sci.* 50 (2005) 511–678, <https://doi.org/10.1016/j.pmatsci.2004.10.001>.
- [23] U. Aschauer, R. Braddell, S.A. Brechbühl, P.M. Derlet, N.A. Spaldin, Strain-induced structural instability in FeRh, *Phys. Rev. B* 94 (2016), 014109, <https://doi.org/10.1103/PhysRevB.94.014109>.
- [24] T. Fukuda, T. Kakeshita, Martensitic transformation in Pd doped FeRh exhibiting a metamagnetic transition, *J. Alloys Compd.* 563 (2013) 192–196, <https://doi.org/10.1016/j.jallcom.2013.02.029>.
- [25] S. Yuasa, H. Miyajima, Y. Otani, Magneto-volume and tetragonal elongation effects on magnetic phase transitions of body-centered tetragonal $\text{FeRh}_{1-x}\text{Pt}_x$, *J. Phys. Soc. Jpn.* 63 (1994) 3129–3144, <https://doi.org/10.1143/JPSJ.63.3129>.
- [26] J. Kim, R. Ramesh, N. Kioussis, Revealing the hidden structural phases of FeRh, *Phys. Rev. B* 94 (2016), 180407, <https://doi.org/10.1103/PhysRevB.94.180407>.
- [27] Y. Hao, L. Zhang, J. Zhu, The electronic structure, phase transition, elastic, thermodynamic, and thermoelectric properties of FeRh: high-temperature and high-pressure study, *Z. Naturforsch. A* 75 (2020) 789–801, <https://doi.org/10.1515/zna-2020-0155>.
- [28] N.A. Zarkevich, D.D. Johnson, FeRh ground state and martensitic transformation, *Phys. Rev. B* 97 (2018), 014202, <https://doi.org/10.1103/PhysRevB.97.014202>.
- [29] R. Oshima, F. Hori, Y. Kibata, M. Komatsu, M. Kiritani, Defect structures and phase transitions of FeRh alloys deformed at high speed deformation, *Mater. Sci. Eng. A* 350 (2003) 139–144, [https://doi.org/10.1016/S0921-5093\(02\)00715-3](https://doi.org/10.1016/S0921-5093(02)00715-3).
- [30] A.R. Yavari, E. Navarro, H. Mori, H. Yasuda, A. Hernando, W.J. Botta, On the B2 \rightarrow FCC transformation of Fe–Rh during deformation, *Philos. Mag. A* 80 (2000) 1779–1793, <https://doi.org/10.1080/01418610008219084>.
- [31] E. Navarro, M. Multigner, A.R. Yavari, A. Hernando, The spin glass state of metastable FCC FeRh, *Europhys. Lett.* 35 (1996) 307, <https://doi.org/10.1209/epl/i1996-00571-0>.
- [32] X. Ye, N. Fortunato, A. Sarkar, H. Geßwein, D. Wang, X. Chen, B. Eggert, H. Wende, R.A. Brand, H. Zhang, H. Hahn, R. Kruk, Creating a ferromagnetic ground state with Tc above room temperature in a paramagnetic alloy through non-equilibrium nanostructuring, *Adv. Mater.* 34 (2022), 2108793, <https://doi.org/10.1002/adma.202108793>.
- [33] J.M. Lommel, J.S. Kouvel, Effects of mechanical and thermal treatment on the structure and magnetic transitions in FeRh, *J. Appl. Phys.* 38 (1967) 1263–1264, <https://doi.org/10.1063/1.1709570>.
- [34] V. Paidar, Displacive processes in systems with BCC parent lattice, *Prog. Mater. Sci.* 56 (2011) 841–851, <https://doi.org/10.1016/j.pmatsci.2011.01.009>.
- [35] L. Rangel DaCosta, H.G. Brown, P.M. Pelz, A. Rakowski, N. Barber, P. O'Donovan, P. McBean, L. Jones, J. Ciston, M.C. Scott, C. Ophus, Prismatic 2.0 – simulation software for scanning and high resolution transmission electron microscopy (STEM and HRTEM), *Micron* 151 (2021), 103141, <https://doi.org/10.1016/j.micron.2021.103141>.
- [36] C. Ophus, A fast image simulation algorithm for scanning transmission electron microscopy, *Adv. Struct. Chem. Imaging* 3 (2017) 13, <https://doi.org/10.1186/s40679-017-0046-1>.
- [37] K. Momma, F. Izumi, VESTA 3 for three-dimensional visualization of crystal, volumetric and morphology data, *J. Appl. Crystallogr.* 44 (2011) 1272–1276, <https://doi.org/10.1107/S0021889811038970>.
- [38] K. Fisher, E. Marquis, Comparing plasma-FIB and Ga-FIB preparation of atom probe tomography samples, Supplement S3Proceedings of the Microscopy and Microanalysis, *Microsc. Microanal.* 22 (2016) 692–693, <https://doi.org/10.1017/S1431927616004311>. Supplement S32016.
- [39] B. Gault, A.J. Breen, Y. Chang, J. He, E.A. Jägle, P. Kontis, P. Kürsteiner, A.K. da Silva, S.K. Mäkinen, I. Mouton, Z. Peng, D. Ponge, T. Schwarz, L.T. Stephenson, A. Szczepaniak, H. Zhao, D. Raabe, Interfaces and defect composition at the near-atomic scale through atom probe tomography investigations, *J. Mater. Res.* 33 (2018) 4018–4030, <https://doi.org/10.1557/jmr.2018.375>.
- [40] B. Gault, A. Chirramonti, O. Cojocaru-Mirédin, P. Stender, R. Dubosq, C. Freysoldt, S.K. Mäkinen, T. Li, M. Moody, J.M. Cairney, Atom probe tomography, *Nat. Rev. Methods Primer* 1 (2021) 1–30, <https://doi.org/10.1038/s43586-021-00047-w>.
- [41] D. Alfé, PHON: a program to calculate phonons using the small displacement method, *Comput. Phys. Commun.* 180 (2009) 2622–2633, <https://doi.org/10.1016/j.cpc.2009.03.010>.
- [42] G. Kresse, J. Furthmüller, Efficient iterative schemes for ab initio total-energy calculations using a plane-wave basis set, *Phys. Rev. B* 54 (1996) 11169–11186, <https://doi.org/10.1103/PhysRevB.54.11169>.
- [43] G. Kresse, D. Joubert, From ultrasoft pseudopotentials to the projector augmented-wave method, *Phys. Rev. B* 59 (1999) 1758–1775, <https://doi.org/10.1103/PhysRevB.59.1758>.
- [44] J.P. Perdew, K. Burke, M. Ernzerhof, Generalized gradient approximation made simple, *Phys. Rev. Lett.* 77 (1996) 3865–3868, <https://doi.org/10.1103/PhysRevLett.77.3865>.
- [45] M. Methfessel, A.T. Paxton, High-precision sampling for brillouin-zone integration in metals, *Phys. Rev. B* 40 (1989) 3616–3621, <https://doi.org/10.1103/PhysRevB.40.3616>.
- [46] S. Ener, J. Neuhaus, W. Petry, R. Mole, K. Hradil, M. Siewert, M.E. Gruner, P. Entel, I. Titov, M. Acet, Effect of temperature and compositional changes on the phonon properties of Ni–Mn–Ga shape memory alloys, *Phys. Rev. B* 86 (2012), 144305, <https://doi.org/10.1103/PhysRevB.86.144305>.
- [47] A. Castets, D. Tochetti, B. Hennion, Spin wave spectrum of iron-rhodium alloy in antiferromagnetic and ferromagnetic phases, *Phys. B+C* 86 (88) (1977) 353–355, [https://doi.org/10.1016/0378-4363\(77\)90344-8](https://doi.org/10.1016/0378-4363(77)90344-8).
- [48] W. Petry, A. Heimig, J. Trampenau, M. Alba, C. Herzig, H.R. Schober, G. Vogl, Phonon dispersion of the bcc phase of group-IV metals. I. BCC titanium, *Phys. Rev. B* 43 (1991) 10933–10947, <https://doi.org/10.1103/PhysRevB.43.10933>.
- [49] H. Okamoto, Fe–Rh (Iron–Rhodium), *J. Phase Equilib. Diffus.* 32 (2011) 472, <https://doi.org/10.1007/s11669-011-9934-6>.
- [50] Y. Kibata, F. Hori, R. Oshima, M. Komatsu, M. Kiritani, Defect structures of intermetallic FeRh alloys induced by high-speed deformation, *MRS Online Proc. Libr.* 753 (2003) 538, <https://doi.org/10.1557/PROC-753-BB5.38>.
- [51] A.R. Yavari, D. Negri, E. Navarro, A. Deriu, A. Hernando, W.J.B. Filho, Deformation induced transformations of B2 FeAl and FeRh, *J. Metastable Nanocryst. Mater.* 2 (6) (1999) 229–236, <https://doi.org/10.4028/www.scientific.net/JMN.2-6.229>.
- [52] M. Matsuda, R. Yamashita, S. Tsurekawa, K. Takashima, M. Mitsuhashi, M. Nishida, Antiphase boundary-like structure of B19' martensite via R-phase transformation in Ti–Ni–Fe Alloy, *J. Alloys Compd.* 586 (2014) 87–93, <https://doi.org/10.1016/j.jallcom.2013.10.015>.
- [53] M. Matsuda, Y. Shinagawa, K. Takashima, M. Mitsuhashi, M. Nishida, Characterization of antiphase boundary-like structure of B33 martensite in Zr–Co–Pd alloy, *Mater. Trans.* 59 (10) (2018) 1567–1573, <https://doi.org/10.2320/matertrans.M2018146>.
- [54] Y. Xu, H. Liu, D. Yi, Z. Zhu, F. Zheng, Antiphase boundary-like structure in α' martensite of TC21 titanium alloy, *Trans. Nonferr. Met. Soc. China* 22 (6) (2012) 1366–1371, [https://doi.org/10.1016/S1003-6326\(11\)61327-7](https://doi.org/10.1016/S1003-6326(11)61327-7).
- [55] R.P. Reed, Martensitic Phase Transformations, *Materials at Low Temperatures*, ASM International, 1983, pp. 295–341, <https://doi.org/10.31399/asm.tb.mlt.t62860295>. Edited by R.P. Reed, A.F. Clark.
- [56] M. Ohring, 9-How engineering materials are strengthened and toughened, *Editor (s): M. Ohring. Engineering Materials Science*, Academic Press, 1995, pp. 431–500. ISBN 9780125249959.
- [57] L. Xuemin, T.Y. Hsu, X. Zuyao, *In situ* study of phase transformations in a 50.8 at.% Ni–Ti alloy, *Metallurgy* 20 (1) (1987) 47–59, [https://doi.org/10.1016/0026-0800\(87\)90064-4](https://doi.org/10.1016/0026-0800(87)90064-4).
- [58] P. Wang, Z. Song, Y. Lin, Q. Li, H. Wang, The nucleation mechanism of martensite and its interaction with dislocation dipoles in dual-phase high-entropy alloys, *J. Alloys Compd.* 909 (2022), 164685, <https://doi.org/10.1016/j.jallcom.2022.164685>.